

#### **OPEN ACCESS**

EDITED BY Majed Katati, University of Granada, Spain

REVIEWED BY
Wei-Chan Hsu,
Friedrich Schiller University Jena, Germany
Subhash Chandra Pal,
IIT Mandi iHub and HCI Foundation, India

\*CORRESPONDENCE
Hai Jin

☑ kingsea300809@163.com
Ligang Chen
☑ clg201820271@126.com
Jing Li
☑ xiaojingzi202@163.com
He Ma
☑ mahe@bmie.neu.edu.cn

RECEIVED 13 June 2025 ACCEPTED 26 September 2025 PUBLISHED 13 October 2025

#### CITATION

Liu R, Zhang R, Qian W, Liang G, Chu G, Jin H, Chen L, Li J and Ma H (2025) Intracranial aneurysm segmentation on digital subtraction angiography: a retrospective and multi-center study. *Front. Neurol.* 16:1646517. doi: 10.3389/fneur.2025.1646517

#### COPYRIGHT

© 2025 Liu, Zhang, Qian, Liang, Chu, Jin, Chen, Li and Ma. This is an open-access article distributed under the terms of the Creative Commons Attribution License (CC BY). The use, distribution or reproduction in other forums is permitted, provided the original author(s) and the copyright owner(s) are credited and that the original publication in this journal is cited, in accordance with accepted academic practice. No use, distribution or reproduction is permitted which does not comply with these terms.

# Intracranial aneurysm segmentation on digital subtraction angiography: a retrospective and multi-center study

Ruibo Liu<sup>1,2</sup>, Ruixuan Zhang<sup>1,2</sup>, Wei Qian<sup>1</sup>, Guobiao Liang<sup>2</sup>, Guangxin Chu<sup>2</sup>, Hai Jin<sup>2\*</sup>, Ligang Chen<sup>2\*</sup>, Jing Li<sup>3\*</sup> and He Ma<sup>1\*</sup>

<sup>1</sup>College of Medicine and Biological Information Engineering, Northeastern University, Shenyang, Liaoning, China, <sup>2</sup>Department of Neurosurgery, General Hospital of Northern Theater Command, Shenyang, Liaoning, China, <sup>3</sup>Department of Neurology, The Fourth Affiliated Hospital of China Medical University, Shenyang, Liaoning, China

**Introduction:** Accurate segmentation of intracranial aneurysms (IAs) in digital subtraction angiography (DSA) is critical for endovascular embolization and risk assessment of ruptured IAs. However, this task remains challenging due to problems like vascular overlap, small target size and similarity to ring blood vessels. To develop a novel deep learning model to improve segmentation performance of IAs on DSA datassets, especially addressing challenges of small IAs.

**Methods:** We propose a novel deep learning model, the Shape-aware dual-stream attention network (SDAN). This network integrates two novel modules: (1) Edge-aware Local Attention Module (ELAM), which differentiates aneurysms from adjacent vasculature by capturing morphological features, (2) Global Shape-aware Fusion Block (GSFB) that enhances pattern recognition through contextual aggregation between domains. The model was trained and tested on 62,187 retrospective DSA images from three institutions, with external validation on 26,415 images. Performance was evaluated using DSC, HD95, and sensitivity. **Results:** The proposed SDAN outperforms the other models when tested on multiple centers separately with an average Dice score of 0.951 on the internal test set and 0.944 on the external test set. We also evaluated the different sizes of aneurysms individually and the results show that SDAN outperforms the other models on all sizes of aneurysms. This study demonstrates the effectiveness of SDAN for intracranial aneurysm segmentation.

**Conclusion:** Our proposed SDAN significantly improves the accurate segmentation of intracranial aneurysms in DSA images beyond existing medical image segmentation models. The model solves the problems of small intracranial aneurysms that are not easily segmented accurately, over-segmentation caused by the similarity of intracranial aneurysms and ring vessels, and under-segmentation caused by the overlap of neighboring vessels.

#### KEYWORDS

intracranial aneurysms, digital subtraction angiography, deep learning, edge-aware local attention, global shape-aware fusion block

# 1 Introduction

Intracranial aneurysms (IAs) represent a critical cerebrovascular pathology, with rupture leading to aneurysmal subarachnoid hemorrhage (aSAH). This condition carries a devastating mortality rate exceeding 50% (1–3). Survivors frequently suffer severe neurological deficits, imposing significant burdens on global healthcare systems (4). Endovascular embolization has emerged as a primary therapeutic intervention; however, its efficacy critically depends on precise IA delineation for preoperative planning and intraoperative navigation (5, 6). Substantially, inaccurate segmentation may compromise the success of interventional treatments (such as endovascular coiling), thereby increasing the risk of perioperative complications like coil protrusion or incomplete occlusion (7). This highlights that sub-millimeter precision is essential in clinical workflows (8).

Current reliance delineation by on manual neurointerventionists is prohibitively slow (> 1.5 minutes per frame) and exhibits substantial variability, particularly for small aneurysms (diameter < 3mm) and in cases of vascular overlap or occlusion (9, 10). This inefficiency delays critical interventions and elevates patient risk during time-sensitive procedures, highlighting the urgency for automated segmentation solutions. Digital subtraction angiography (DSA) remains the gold standard for IA characterization due to its superior spatial resolution (150 -  $200\mu m/pixel$ ) and clear depiction of vascular anatomy, making it indispensable for intraoperative guidance (11-13). In contrast, computed tomography angiography (CTA) and magnetic resonance angiography (MRA) are more widely adopted for screening owing to their noninvasive nature, with datasets often including patients without aneurysms to reflect real-world clinical scenarios (14, 15). However, these modalities are susceptible to motion artifacts and offer lower temporal resolution, limiting their utility in complex interventional settings.

The lack of segmentation tools that are accurate, capable of real-time operation, and sensitive to small IAs for single-frame 2D DSA represents a critical gap. Furthermore, the clinical translation of existing models is hindered by insufficient validation on large-scale, multi-center DSA datasets. To address these limitations, this study introduces the Shape-aware Dual-stream Attention Network (SDAN), explicitly designed for accurate IA segmentation. Our innovations include: (1) Edge-aware Local Attention Module (ELAM): A learnable edge detection module combining Canny operator with convolutions and local attention to capture morphological features, addressing the problem of distinguishing IAs from adjacent vasculature; (2) Global Shape-aware Fusion Block (GSFB): A cross-dimensional feature aggregator integrating spatial-channel attention mechanisms, enabling robust recognition through hemodynamic context modeling.

We trained and evaluated SDAN on a retrospective dataset comprising 62,187 DSA images from three independent institutions. Our objective is to deliver a clinically viable segmentation tool that significantly outperforms existing state-of-the-art methods, particularly for small IAs, thereby enabling faster, safer, and more precise endovascular interventions.

# 2 Related work

# 2.1 Clinical challenges in accurate segmentation of IAs

The segmentation of intracranial aneurysms (IAs) remains a high-stakes clinical challenge where computational precision directly affects procedural safety. Prior studies establish that geometric discrepancies exceeding 1 mm between segmented and true aneurysm morphology correlate with increased intraoperative complications (7), underscoring the need for submillimeter precision in real-world embolization workflows. This demand is particularly acute for small IAs (< 3mm diameter), which exhibit higher misclassification rates due to limited contrast retention and overlapping vasculature (10). While recent consensus guidelines highlight IA segmentation as critical for minimizing perioperative risks (5), conventional approaches relying on manual delineation or threshold-based techniques lack the requisite spatial fidelity and speed for intraoperative adoption.

# 2.2 Limitations of current computational approaches

Deep learning has shown promise in addressing medical image segmentation challenges, but existing IA-related studies exhibit clear modality biases (16, 17). For DSA-based approaches, early efforts include Jerman et al.'s work (18), which computed intravascular distance maps from 3D-DSA images for CNN-based classification but suffered from high computational overhead. Podgorsak et al. (19, 20) modified VGG networks to achieve threeclass segmentation (background, vasculature, and aneurysm) in DSA with good agreement between predictions and ground truth. Duan et al. (21) proposed a two-stage CNN architecture integrating frontal and lateral views with false-positive suppression to improve detection specificity. For 2D+time DSA sequences, Jin et al. (22) developed a U-shaped network incorporating spatiotemporal information, achieving 89.3% sensitivity but with 3.77 average false positives per sequence, while Liao et al. (23) combined CNNs with ConvLSTM to capture temporal dynamics, enhancing accuracy through multi-frame fusion.

Meanwhile, numerous studies focus on CTA/MRA or 3D rotational angiography (3D-RA) (24, 25). Zhang et al. (26) proposed FSTIF-UNet with feature fusion and attention mechanisms, showing improved performance on 3D-RA for complex vasculature and small aneurysms, though 3D-RA requires multi-angle acquisitions with 17.6-22.2 second processing delays (27–29), rendering it unsuitable for real-time guidance. CTA-specific models (9, 30–32) demonstrate robust detection but are tailored to CT imaging characteristics.

Despite these advancements, critical limitations persist. Conventional 2D DSA segmentation algorithms degrade significantly when vascular overlap exceeds 50% (33), and most deep learning approaches—including DSA-specific ones—exhibit poor performance on small IAs, which constitute over 30% of multi-center cases (21, 23, 34) and whose misidentification

impacts rupture risk assessment. Additionally, many studies suffer from limited dataset size, narrow aneurysm type diversity, and sensitivity to DSA image quality variations caused by contrast injection parameters.

Existing deep learning solutions for IA analysis prioritize modalities like CTA and MRA (13, 35), despite DSA's established role as the gold standard for vascular characterization. Methods designed specifically for DSA face three interrelated constraints:

- Temporal Incompatibility: 3D rotational angiography achieves moderate segmentation accuracy (Dice: 0.87–0.90) but requires multi-angle acquisitions incompatible with single-frame navigation needs (27).
- Contextual Blind Spots: Hybrid frameworks (36) integrate symbolic rules with deep networks but fail to model hemodynamic context in overlapping vessels, leading to false positives in > 40% of small IAs.
- Morphological Rigidity: Graph-based refinements (37) improve boundary delineation yet remain sensitive to aneurysm shape irregularity—a key predictor of rupture risk neglected in current benchmarks.

# 2.3 Insights from non-DSA vascular segmentation and DSA-specific challenges

Insights from non-DSA vascular segmentation suggest promising avenues for innovation. The integration of learnable edge detectors with attention mechanisms (38) demonstrates enhanced sensitivity to tubular structures in retinal imaging, while dual-path feature fusion (39) mitigates noise in low-dose CT angiography. However, these approaches lack optimization for DSA's projective geometry, where depth ambiguity amplifies topological complexity. Similarly, unsupervised shape modeling techniques (31) reduce annotation dependency but cannot resolve the signal-to-noise limitations inherent in DSA's subtraction artifacts.

# 3 Materials and methods

## 3.1 Dataset collection and preprocessing

This study retrospectively collected 62,187 DSA images from three medical centers between 2013 and 2024. The dataset included: Northern Theater Command General Hospital (Institution 1: 35,772 images from 655 patients), 242 hospital affiliated to Shenyang Medical College (Institution 2: 14,055 images from 247 patients) and the Fourth Affiliated Hospital of China Medical University (Institution 3: 12,360 images from 212 patients). All images were acquired using 300mgI/mL iodinated contrast agent (Schering AG) with a spatial resolution of 0.308  $\times$  0.308 mm and matrix sizes ranging from 960  $\times$  960 to 1,240  $\times$  1,240 pixels. The details of data collection and preprocessing is illustrated in Figure 1. Characteristics of the dataset are listed in Table 1. We divided data from Institution 1 into training set and internal test set with a ratio of 8:2, while data from Institution 2 and Institution 3 are used as external test sets. The mean age of the patient was 57.65

years (interquartile range [IQR]: 42–86 years), with balanced sex distribution (56.53% female) and the aneurysms demonstrated a diameter skewness (24.37% small aneurysms  $<3mm,\,9.65\%$  large aneurysms >10mm) distributed across critical vascular territories, including the internal carotid artery (17.72%) and the middle cerebral artery (20.25%) (P<0.001). The equipment models are listed in Table 2. To address multicenter scanner variations, at the preprocessing stage, for each image from DSA sequences, we first utilized CLAHE to improve the contrast of vascular structure. Subsequently, we resized images to 512  $\times$  512 to unify the shape of all images.

# 3.2 Research strategy and model architecture

Collectively, prior work reveals a persistent challenge: No framework simultaneously addresses the spatial-temporal constraints of DSA (single frame processing), morphological variability, and clinical deployability. To address this challenge, we developed the Shape-aware Dual-stream Attention Network (SDAN). The design of the network is based on observations of neurointerventional decision making, where clinicians combine local edge discontinuities, such as aneurysm neck morphology, with a global hemodynamic context, including the trajectory of the parent vessel, to determine the location of an intracranial aneurysm. The structure of SDAN is shown in Figure 1b, which incorporates a convolutional patch embedding module as the initial feature extraction step (40). This module replaces traditional patch embedding with task-oriented convolutional operations to reduce computational overhead. This embedding method retains more local image information, thereby improving the effectiveness of feature extraction. Notably, the first feature map undergoes 4× downsampling (rather than 2×) to balance spatial resolution retention with computational efficiency. Given the high native resolution of the DSA images, scaling 4× compresses redundant background information while preserving critical morphological details of small aneurysms and vessel edges. Subsequently, two main modules are designed: Edge-aware Local Attention Module (ELAM) and Global Shape-aware Fusion Block (GSFB). Detailed architectural configurations and functional mechanisms of these components will be elaborated in the subsequent sections.

# 3.3 Edge-aware local attention module

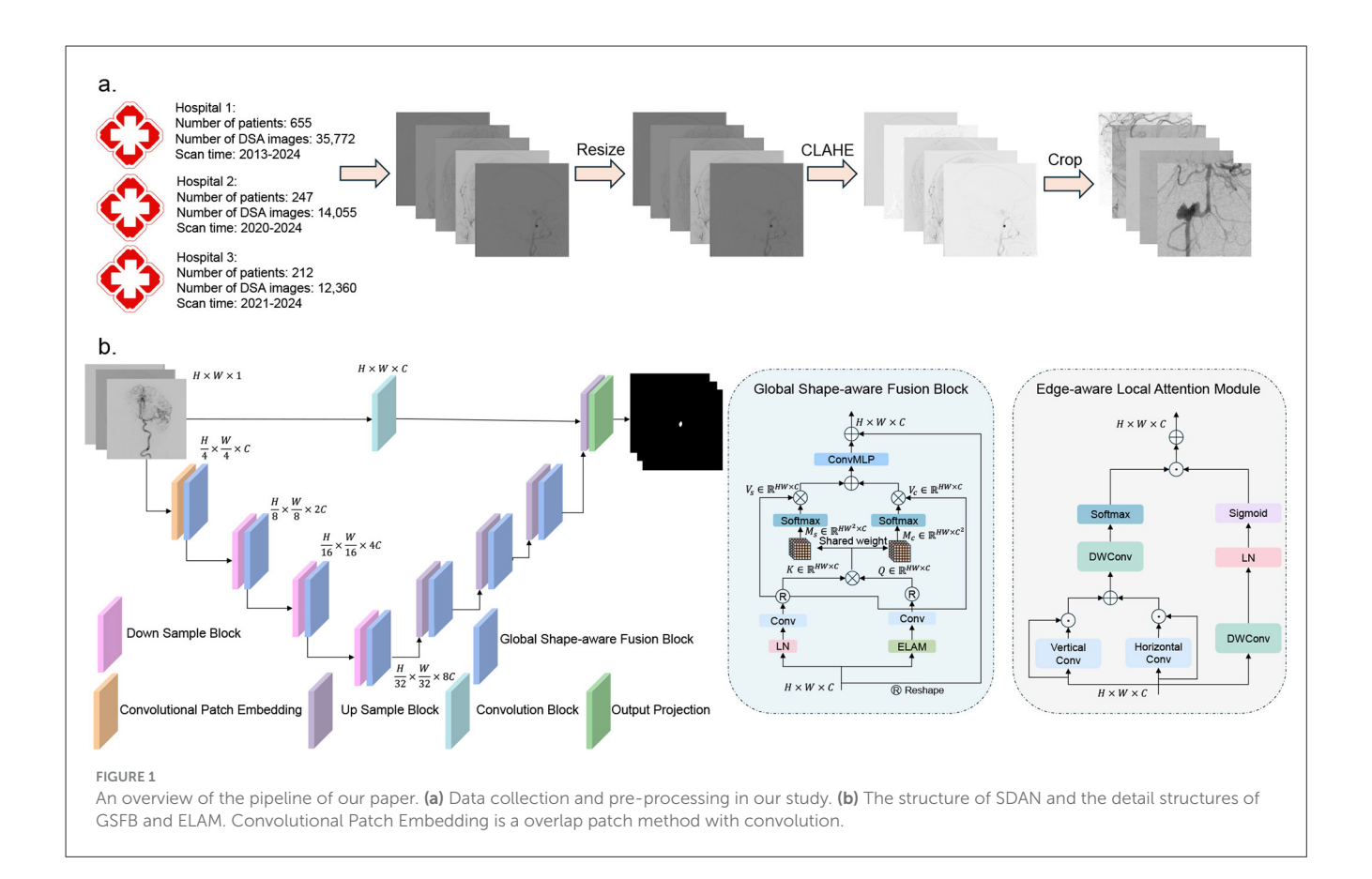
Since human blood vessels are topologically oriented, we transform the gradient computation principle of the classical Canny edge detection operator into a learnable convolutional form to extract anisotropic features of the vascular structure:

$$F_h = K_h \cdot X, \tag{1}$$

$$F_{\nu} = K_{\nu} \cdot X, \tag{2}$$

where  $K_h$  and  $K_{\nu}$  are the horizontal and vertical convolution kernels with kernel size of 3  $\times$  3, respectively. The boundary

10 3389/fneur 2025 1646517 Liu et al.



enhancement mechanism of the visual system is then simulated using matrix addition:

$$F = F_h + F_{\nu}. (3)$$

And the spatial attention weights are generated by depthseparable convolution  $\mathcal{D}$ , where the Sigmoid function  $\sigma$  is able to constrain the weight range to [0, 1]:

$$A = \sigma(\mathcal{D}(F)),\tag{4}$$

Meanwhile, X is processed through  $\mathcal{D}$  and Layer Normalization (LN) to obtain the channel-related features  $F_c$ . Then A is weighted onto  $F_c$  to obtain the result features:

$$F_c = LN(\mathcal{D}(X) + X), \tag{5}$$

$$F_{ELAM} = F_c \odot A + X, \tag{6}$$

here, ⊙ denotes element-wise multiplication. The design enables ELAM to adaptively focus on morphological discontinuites in the vessel wall, overcoming the shortcoming of traditional fixation operators that are sensitive to biological tissue variability.

## 3.4 Global shape-aware fusion block

Since ELAM is a form of local attention, it causes the network to focus only on features within the receptive field, making it highly sensitive to noise and subtle changes in vascular structures (41, 42). Therefore, we introduced Global Shape-aware Fusion Block (GSFB), a global attention mechanism that combines spatial and channel dimensions. It can map local attention into global attention, reducing sensitivity of the model to noise and enhancing its robustness to slight changes in vascular structures, thereby enabling the acquisition of aneurysm features, as illustrated in Figure 1b. GSFB consists of spatial global attention and channel global attention, utilizing Convolutional Multilayer Perceptron (ConvMLP) to mix these features. First, the output of ELAM  $(F_{ELAM})$ , is utilized as query (Q), which contains localized shape features. The key (K), spatial value  $(V_s)$ , and channel value  $(V_c)$ are extracted from the input features, ensuring the consistency and stability of the features. In particular, weight sharing between Q and K is used to reduce computational complexity while maintaining feature alignment. Second, spatial and channel dimensional multihead attention are processed separately:

$$MHA_{s} = softmax(\frac{QK^{T}}{\sqrt{d_{k}}}V_{s}), \tag{7}$$

$$MHA_{c} = softmax(\frac{QK^{T}}{\sqrt{d_{k}}}V_{c}), \tag{8}$$

$$MHA_c = softmax(\frac{QK^T}{\sqrt{d_k}}V_c), \tag{8}$$

where  $d_k$  is the key dimension and MHA means multi-head attention. For spatial attention, the computation focuses on interregion dependencies, while channel attention emphasizes feature channel relationships. This approach enables GSFB to capture both global structural patterns and fine-grained local features. Finally, the output features from spatial and channel branches are mixed through a ConvMLP:

TABLE 1 Basic information and statistical analysis of the dataset.

Characteristics	Training and in	nternal test set	External	<i>P</i> Value <sup>‡</sup>	
	Training set	Internal test set	External test set 1	External test set 2	
Patients	536	119	247	212	
Age (y)*	57.65 (42-84)	55.69 (41–76)	57.70 (41-86)	56.75 (51–75)	0.004
Sex					0.980
Female	303 (56.53%)	78 (58.21%)	142 (57.49%)	120 (56.60%)	
Male	233 (43.47%)	56 (41.79%)	105 (42.51%)	92 (43.40%)	
DSA equipment	2	2	1	1	
DSA images	28,471	7,301	14,055	12,360	
Aneurysms	632	131	285	237	
Aneurysm size					< 0.001
> 10mm	61 (9.65%)	14 (10.69%)	8 (2.81%)	8 (3.38%)	
5 to < 10mm	97 (15.35%)	29 (22.14)	61 (21.40%)	62 (26.16%)	
3 to < 5 mm	320 (50.63%)	40 (30.53%)	101 (35.44%)	92 (38.82%)	
< 3 mm	154 (24.37%)	48 (36.64%)	115 (40.35%)	75 (31.64%)	
Aneurysm location					< 0.001
Internal carotid artery	112 (17.72%)	25 (19.08%)	71 (24.91%)	41 (17.30%)	
Middle cerebral artery	128 (20.25%)	23 (17.56%)	37 (12.98%)	29 (12.24%)	
Anterior cerebral artery	25 (3.96%)	6 (4.58%)	7 (2.46%)	11 (4.64%)	
Anterior communicating artery	124 (19.62%)	15 (11.45%)	51 (17.89%)	38 (16.03%)	
Posterior communicating artery	111 (17.56%)	18 (13.74%)	60 (21.05%)	62 (26.16%)	
Posterior cerebral artery	22 (3.48%)	9 (6.87%)	15 (5.26%)	12 (5.06%)	
Vertebral artery	45 (7.12%)	11 (8.40%)	16 (5.61%)	20 (8.44%)	
Basilar artery	35 (5.54%)	10 (7.63%)	7 (2.46%)	11 (4.64%)	
Other †	30 (4.75%)	14 (10.69%)	21 (7.38%)	13 (5.49%)	

 $<sup>^*</sup>$ Data are mean value; data in parentheses are IQRs.

TABLE 2 List of equipment models.

Institution	Equipment model
Institution 1	SIEMENS AXIOM Artis system, Philips Azurion 5M20
Institution 2	SIEMENS AXIOM Artis system
Institution 3	GE MEDICAL SYSTEMS

$$F_{fusion} = MHA_s + MHA_c + LN(X), (9)$$

$$F_{out} = F_{fusion} + ConvMLP(F_{fusion}) + X, \tag{10}$$

where ConvMLP is defined as two convolutions connected with ReLU function, dynamically fuses multi-scale features and suppresses noise by leveraging global context.

Firstly, by extending receptive fields to the entire feature map, GSFB mitigates the over-sensitivity of ELAM to local noise, a limitation observed in traditional local attention mechanisms. Secondly, dual-stream attention ensures sensitivity to vascular deformations and maintain robustness to the diverse shapes of vascular structures, enabling the network to focus on extracting the features of IAs. Thirdly, Weight sharing and parallel spatial-channel processing reduce computational overhead, aligning with the efficiency goals of modern attention architectures (43). The refined architecture balances computational efficiency with medical image analysis tasks especially for specific structures.

# 3.5 Loss function

ELAM and GSFB leverage edge-aware features to improve the ability to identify aneurysms. We seek to augment regional discriminative power of the network with an appropriate loss function design, specifically to dampen its responsiveness to noise and irrelevant edge signals. Thus, we formulate the final loss function as a combination of the Dice and focal losses:

$$\mathcal{L} = 1 - \frac{2|y \cap \hat{y}|}{|y| + |\hat{y}|} - (1 - \hat{y})^2 \log(\hat{y}), \tag{11}$$

<sup>†</sup>Other locations including pericallosal artery, Anterior cerebellar artery, Posterior cerebellar artery, and Anterior choroid aneurysm.

 $<sup>^{\</sup>ddagger}$ Data are considered statistically significant if  $P \leq 0.05$ . P values were calculated using Mann-Whitney U rank test for continuous distributions; discrete distributions were assessed using Kruskal-Wallis H-test.

where *y* is the true label and  $\hat{y}$  is the prediction result.

# 4 Experiment and results

# 4.1 Training and implementation details

In this section, we will introduce the parameters and the implementation details to make sure the reproducibility of SDAN. For the architecture of SDAN, the number of channels in the first layer is 32, and the number of channels in each subsequent layer is twice the number of channels in the previous layer. In addition, the number of channels of skip-connection in the input layer is also 32. Images in training dataset were patched to 224 × 224, while test images were only normalized by CLAHE and the model would predict images by sliding window method, as illustrated in Figure 1a. During the training phase of SDAN, we employed AdamW (44) optimizer with an initial learning rate of 0.0001 to train the model. Besides that, a cosine annealing learning rate schedule was used to decay the learning rate during training. And we set batch size of 8. Our framework is trained and implemented in PyTorch 2.1.1 using a deep learning workstation with two NVIDIA

TABLE 3 Hardware and software environment.

Name	Version
PC System	Ubuntu 24.04 LTS
CPU	Intel(R) Core(TM) i9-14900K
GPU	NVIDIA RTX A6000 $\times$ 2
python	3.10.13
pytorch	2.1.1
monai	1.3.0
timm	0.9.16

RTX A6000. The detail of hardware and software is illustrated in Table 3.

#### 4.2 Evaluation details

We evaluated SDAN and conducted a detailed comparison with some existing models. These models are as follows: UNet (45), UNetV2 (46), Attention-UNet (47), nnUNet (48), SegNet (49), UNETR (50), SwinUNet (51), SwinUNetR (52), VMUNet (53), VMUNetV2 (54), and HTC-Net (39). UNet and other UNet-like models are used to explain the prior performance for GSFB. In particular, Attention-UNet was utilized for IA segmentation in previous research, and HTC-Net was used to balance local and global information. For all methods, we adjusted the hyperparameters to ensure that the optimal results were obtained during the training process.

The performance of SDAN in the IA segmentation task is evaluated by Dice Similarity Coefficient (DSC), 95% Hausdorff Distance (HD95), Sensitivity, Precision, and Intersection over Union (IoU). A paired t-test P value less than 0.05 is considered to indicate a statistically difference. Specifically, DSC measures the overlap between the prediction and the ground truth, which is particularly suitable for evaluating small target segmentation tasks. The calculation method is:

$$DSC = \frac{2 \cdot |A \cap B|}{|A| + |B|} \tag{12}$$

where A represents the prediction and B represents the ground truth. HD95 quantifies the maximum distance between the prediction boundary points and the ground truth, focusing on evaluating the precision of the segmentation boundaries. It is a robust variant of the standard Hausdorff distance, excluding the top 5% of extreme distance values to reduce the impact of outliers. HD can be calculated as follows:

$$HD = \max(\max_{a \in A} \min_{b \in B} ||a - b||, \max_{b \in B} \min_{a \in A} ||b - a||)$$
 (13)

TABLE 4 Model performance on internal test dataset with DSC, HD95, Sensitivity, Precision, and IoU.

	DSC	HD95	Sensitivity	Precision	loU
UNet	0.821	39.249	0.826	0.845	0.745
UNetV2	0.789	9.226	0.754	0.887	0.710
Attention-UNet	0.855	11.981	0.852	0.894	0.792
nnUNet	0.923	2.365	0.931	0.917	0.875
SegNet	0.848	7.995	0.842	0.891	0.783
UNETR	0.716	109.161	0.732	0.739	0.624
SwinUNet	0.726	15.598	0.733	0.779	0.650
SwinUNetR	0.918	53.164	0.940	0.909	0.860
VMUNet	0.857	10.040	0.853	0.885	0.790
VMUNetV2	0.786	11.519	0.769	0.855	0.703
HTC-Net	0.803	11.072	0.786	0.871	0.727
SDAN	0.951	1.995*	0.946*	0.959*	0.908*

The best results are displayed in red, and the second-best results are displayed in blue. \*P values indicate significance compared with nnUNet (P < 0.05).

HD95 thereby can be calculated by selecting the top 95% of the directed distance values.

In addition, sensitivity reflects the model's ability to correctly identify all true target regions, precision measures

the proportion of pixels predicted as target regions that are actually true targets, and IoU evaluates the overlap between the prediction and the ground truth by the ratio of their intersection to their union, providing a stricter measure

TABLE 5 Model performance on external test dataset with DSC, HD95, Sensitivity, Precision, and IoU.

Institution	DSC	HD95	Sensitivity	Precision	IoU
Institution 1	0.951	1.995	0.946	0.959	0.908
Institution 2	0.943	1.873	0.913	0.976	0.892
Institution 3	0.944	1.416	0.913	0.979	0.895

TABLE 6 Performance of ablation studies.

Baseline	ResBlock	ELAM	SE	GSFB	DSC	HD95	Sensitivity	Precision	loU
1					0.764	65.870	0.782	0.789	0.677
1		✓			0.809	21.021	0.813	0.835	0.731
✓	<b>✓</b>	✓			0.804	24.436	0.808	0.833	0.727
✓			1	1	0.797	27.979	0.811	0.811	0.719
1		✓		1	0.951	1.995	0.946	0.959	0.908

The best results are shown in red.

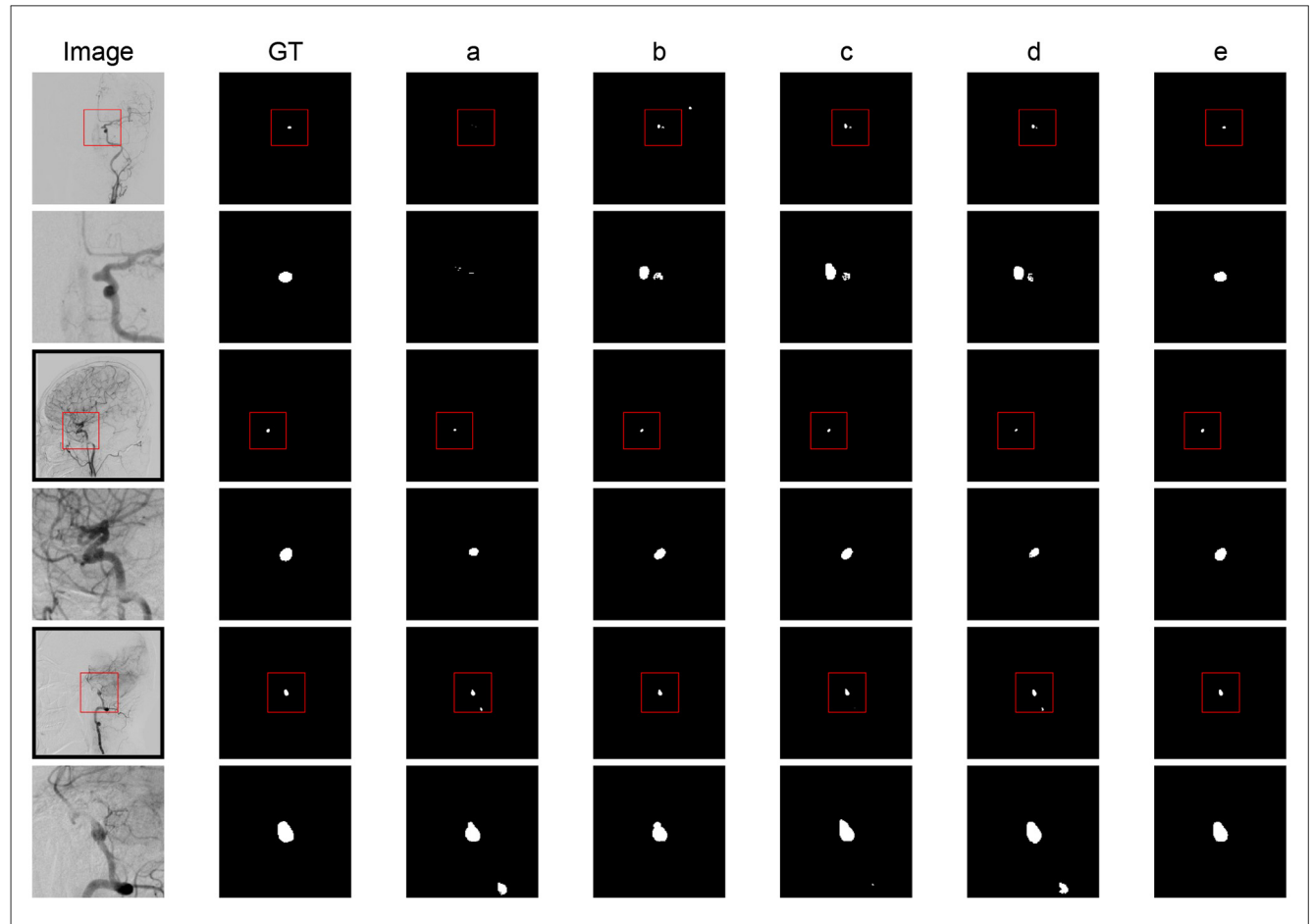


FIGURE 2
Segmentation results comparison of different modules. (a) Baseline model. (b) Baseline + ELAM. (c) Baseline + ELAM + ResBlock. (d) Baseline + SE + GSFB. (e) SDAN.

TABLE 7 Model performance on different sizes of IAs of internal test dataset with DSC, HD95, Sensitivity, Precision, and IoU.

	DSC	HD95	Sensitivity	Precision	loU
Small					
UNet	0.179	76.036	0.442	0.421	0.283
UNetV2	0.273	11.687	0.227	0.595	0.201
Attention-UNet	0.472	18.552	0.455	0.674	0.404
nnUNet	0.863	9.517	0.873	0.852	0.847
SegNet	0.482	12.444	0.498	0.615	0.410
UNETR	0.229	150.857	0.296	0.242	0.161
SwinUNet	0.145	44.002	0.163	0.354	0.111
SwinUNetR	0.844	70.412	0.891	0.829	0.758
VMUNet	0.548	22.456	0.571	0.626	0.454
VMUNetV2	0.342	23.677	0.366	0.503	0.246
HTC-Net	0.365	17.597	0.391	0.863	0.295
SDAN	0.929	1.546*	0.908*	0.957*	0.869*
Middle					
UNet	0.693	27.818	0.703	0.739	0.589
UNetV2	0.558	12.183	0.511	0.769	0.454
Attention-UNet	0.756	9.205	0.737	0.822	0.650
nnUNet	0.892	6.221	0.896	0.901	0.866
SegNet	0.699	9.714	0.700	0.784	0.606
UNETR	0.480	90.420	0.486	0.532	0.381
SwinUNet	0.351	28.309	0.399	0.443	0.275
SwinUNetR	0.889	32.383	0.905	0.889	0.810
VMUNet	0.694	14.762	0.705	0.739	0.596
VMUNetV2	0.538	15.390	0.529	0.686	0.433
HTC-Net	0.603	17.317	0.619	0.697	0.507
SDAN	0.935*	1.441*	0.932*	0.940*	0.878*
Large					
UNet	0.866	35.052	0.867	0.885	0.866
UNetV2	0.862	8.899	0.839	0.916	0.862
Attention-UNet	0.891	10.463	0.899	0.907	0.891
nnUNet	0.931	2.147	0.940	0.938	0.897
SegNet	0.899	7.162	0.896	0.924	0.899
UNETR	0.773	104.903	0.800	0.781	0.773
SwinUNet	0.835	10.859	0.847	0.858	0.835
SwinUNetR	0.923	55.297	0.949	0.908	0.923
VMUNet	0.908	8.270	0.904	0.926	0.908
VMUNetV2	0.856	10.967	0.848	0.894	0.856
HTC-Net	0.868	9.439	0.850	0.912	0.848
SDAN	0.954*	2.002*	0.952*	0.958*	0.954*
Huge					
UNet	0.914	43.086	0.911	0.929	0.851

(Continued)

10 3389/fneur 2025 1646517 Liu et al.

TABLE 7 (Continued)

	DSC	HD95	Sensitivity	Precision	loU
UNetV2	0.911	7.964	0.867	0.967	0.842
Attention-UNet	0.938	14.166	0.927	0.955	0.888
nnUNet	0.943	2.011	0.941	0.946	0.902
SegNet	0.929	7.565	0.910	0.957	0.874
UNETR	0.854	115.485	0.851	0.886	0.764
SwinUNet	0.885	12.902	0.865	0.927	0.807
SwinUNetR	0.942	57.092	0.956	0.934	0.896
VMUNet	0.933	7.918	0.916	0.957	0.879
VMUNetV2	0.906	8.398	0.866	0.960	0.834
HTC-Net	0.907	9.424	0.865	0.966	0.838
SDAN	0.965*	2.471 (p = 0.12)	0.960*	0.971*	0.933*

<sup>\*</sup>P values indicate significance compared with nnUNet (P < 0.05). The best results are displayed in red, and the second-best results are displayed in blue.

of overlap compared to DSC. These metrics are calculated as follows:

Sensitivity = 
$$\frac{TP}{TP + FN}$$
 (14)  
Precision =  $\frac{TP}{TP + FP}$  (15)  

$$IoU = \frac{|A \cap B|}{|A \cup B|}$$
 (16)

$$Precision = \frac{TP}{TD \perp ED} \tag{15}$$

$$IoU = \frac{|A \cap B|}{|A \cup B|} \tag{16}$$

# 4.3 Model performance on internal test dataset

SDAN was evaluated on 7,301 DSA images from internal test dataset. The results are listed in Table 4. The model achieved a DSC of 0.951, surpassing existing methods by 2.83%-23.54%. The HD95 of SDAN reached 1.995, indicating that the contour of SDAN's results is very close to the contour of the ground truth. SDAN also showed the best performance in Sensitivity, Precision, and IoU, indicating that our model has excellent robustness to noise and a high ability to distinguish IAs from adjacent blood vessels. Evidently, SDAN exhibits superior and more concentrated DSC values, signifying it has a better ability to segment the aneurysm region. Moreover, the more outstanding and clustered HD95 metrics demonstrate SDAN's sensitivity to aneurysm contours, along with its superior discriminatory power between aneurysms and adjacent vascular structures.

# 4.4 Model performance on external test dataset

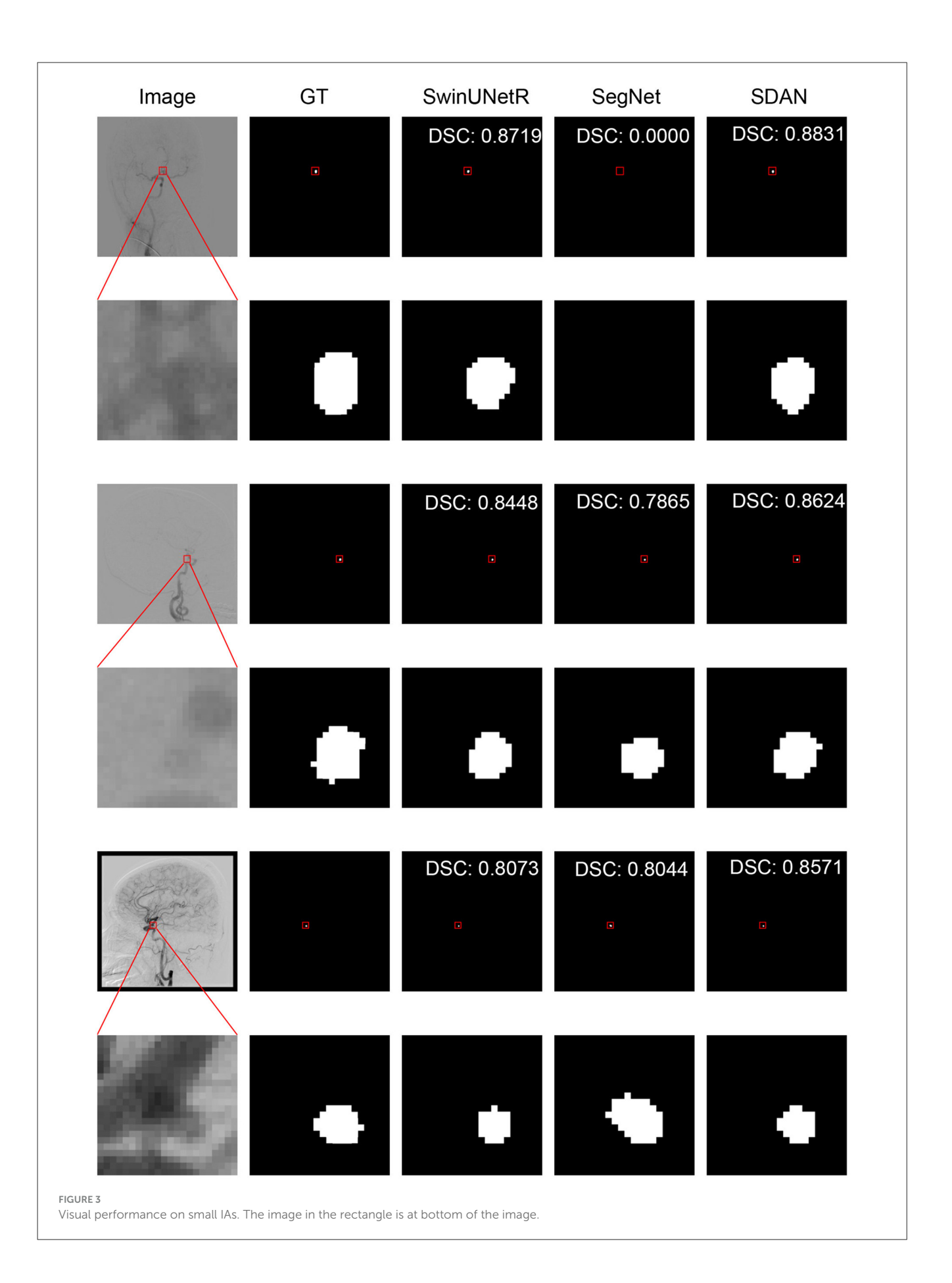
In this section, we evaluated SDAN using our external evaluation datasets. The total results are illustrated in Table 5. Compared with the results of the internal test dataset, our SDAN performed well in the external test datasets and showed consistency with its performance in the internal test dataset. In terms of overall performance, the HD95 of the external test datasets increased by 0.122 and 0.579, while the Precision results improved by 0.017 to 0.02. For results across different diameters, the external test datasets showed small improvements in small and middle IAs (DSC increased by approximately 0.01). Its performance in large and huge IAs was inferior to that in the internal test dataset, with the DSC value decreasing by approximately 0.015, within the error range, SDAN demonstrated a high degree of consistency in performance across all datasets.

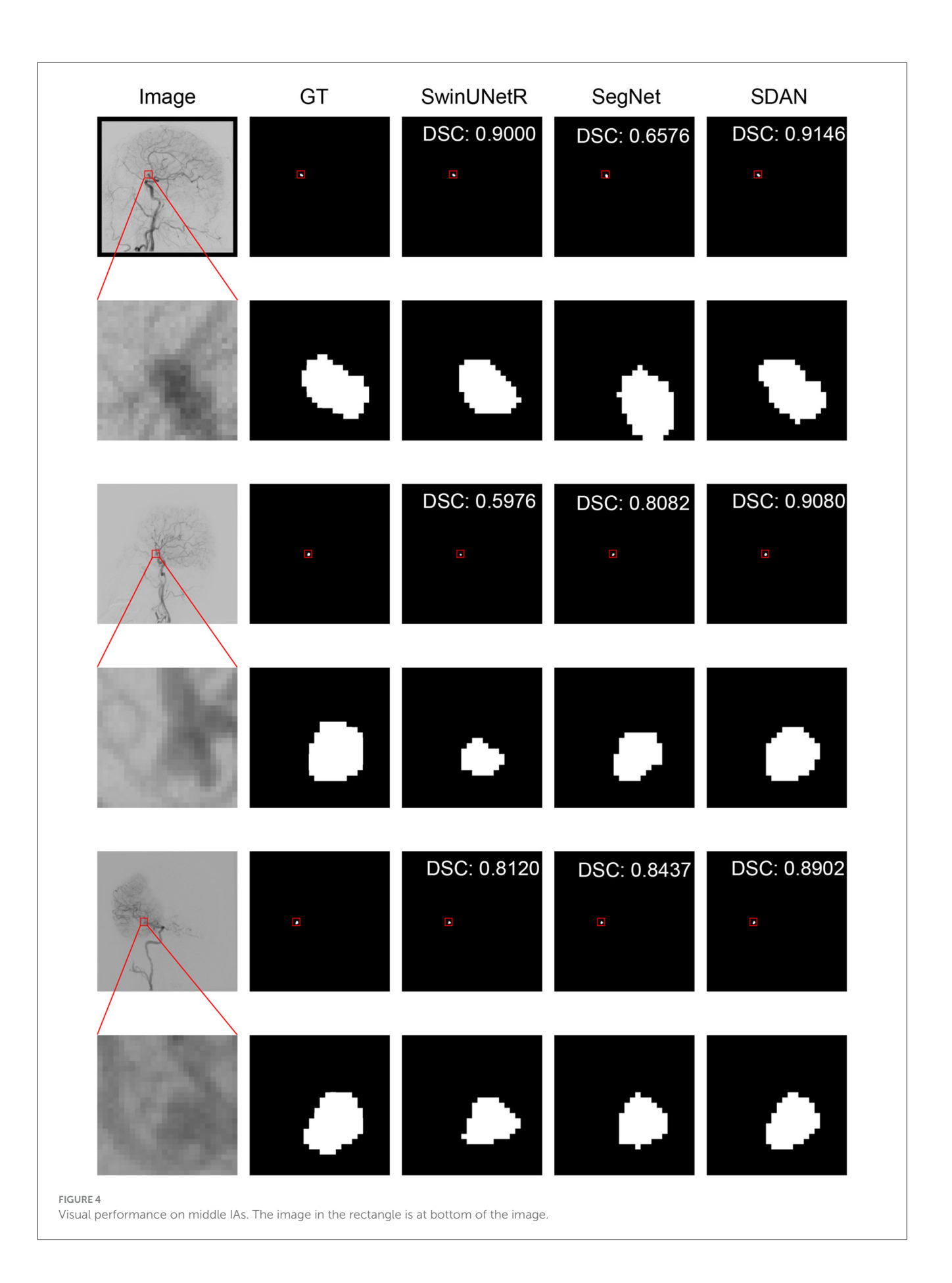
#### 4.5 Ablation studies

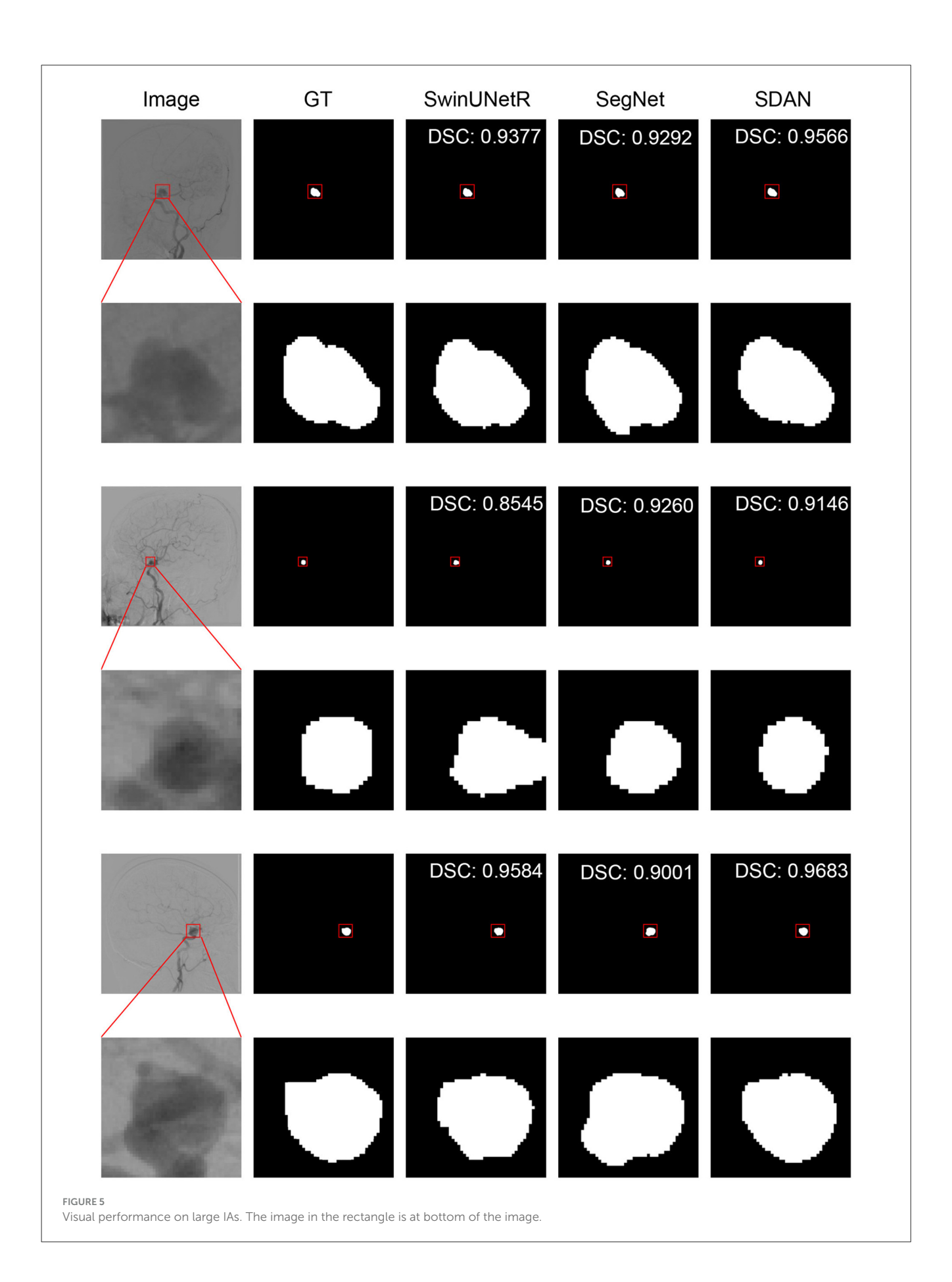
We conducted ablation experiments on SDAN to discuss the effects of the modules in SDAN. Firstly, we replaced ELAM with residual block (ResBlock) as baseline model. Secondly, we used only ELAM as the backbone to show the effect of ELAM. Thirdly, we utilized ResBlock to replace GSFB to illustrate the effect of GSFB in SDAN. Finally, we employed a local attention mechanism, named Squeeze-and-Excitation block (SE) (55) to replace ELAM to show the effect of attention mechanism in ELAM.

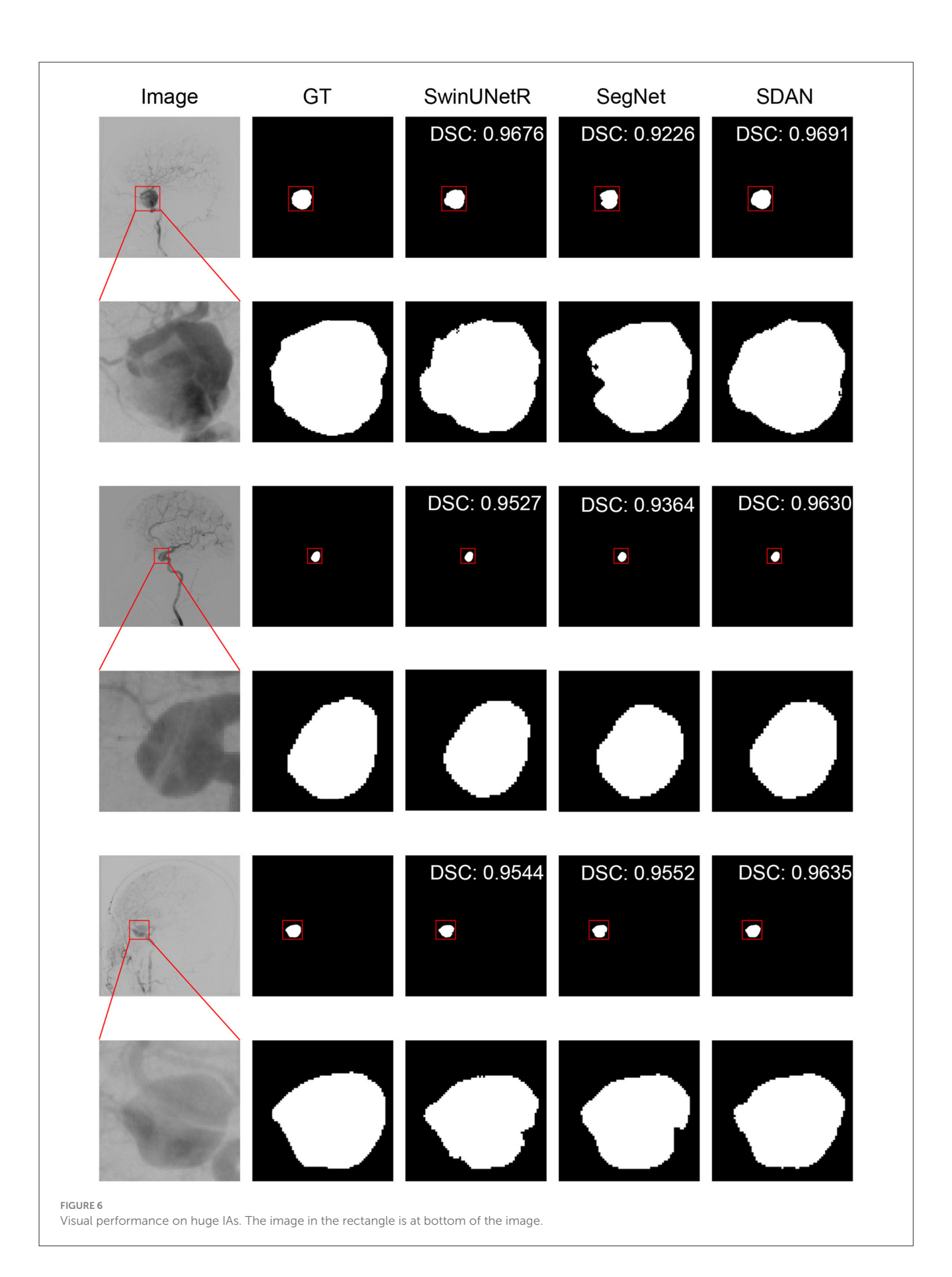
The quantitative results are illustrated in Table 6. The baseline model showed passable performance with DSC of 0.764, and HD95 was 65.870. When ELAM was added, all results improved. It indicated that ELAM could effectively enhance the performance with DSC increased to 0.809. However, when ELAM was combined with ResBlock, DSC decreased slightly to 0.804, suggesting that this combination was less effective than using ELAM alone, and GSFB outperformed ResBlock. When combined with ELAM, DSC increased significantly to 0.951, which was superior to other combinations. Furthermore, when SE was combined with GSFB, the DSC was 0.797. Despite some improvement in results, it was still much lower than the combination of ELAM and GSFB.

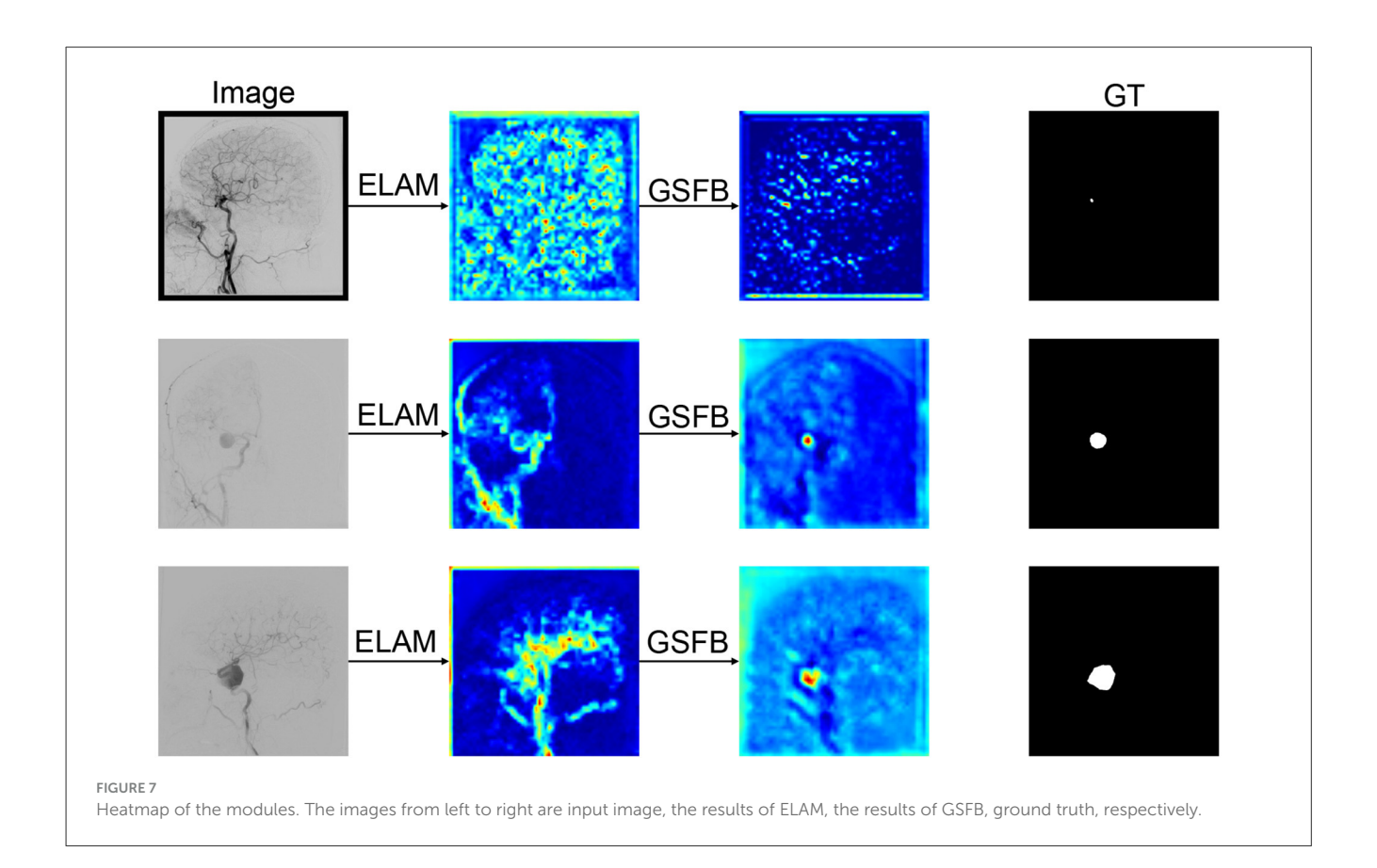
The qualitative results are shown in Figure 2. The baseline models showed a significant deviation from the global truth. The boundaries were unclear with many errors. The result of the combination of baseline and ELAM was obviously improved compared to the baseline model and is closer to the global truth.











The segmentation effect of the combination of ELAM and ResBlock was inferior to that of the use of ELAM alone. The effect of SE was also not as good as that of ELAM.

In general, while ELAM improves aneurysm segmentation performance, it exhibits low contour sensitivity and limited discrimination between aneurysms and adjacent vessels. In contrast, integrating GSFB significantly enhances this discriminatory capacity. These findings validate ELAM's boundary sensitivity and GSFB's discriminative power, aligning with the functional analysis results.

# 5 Discussion

#### 5.1 Performance of different size

We conducted a detailed analysis of the performance of SDAN for different diameters of IAs. Table 7 systematically presents and compares the results of SDAN and other models under the conditions of multi-scale aneurysm diameters. The results show that SDAN demonstrates excellent stability in the segmentation task of small IAs, with a DSC of 0.929, which is significantly superior to the comparative models by 6.6%–78.4%. Except for nnUNet and SwinUNetR, the remaining methods failed to produce valid results. Although the results of nnUNet are relatively high with a DSC of 0.863, there is still a significant gap compared with SDAN. In the scenario of middle IAs, although the performance of each model has improved compared with that in the group of small IAs, SDAN still remains the best results. When dealing with large and huge IAs, all models show good segmentation results,

indicating that the existing methods have reliable processing capabilities for large targets, but generally have shortcomings in segmenting small targets. The visual results are illustrated in Figures 3–6. In these images, we illustrate some common problems for IA segmentation, such as IAs overlapping with blood vessels and IAs with blurred edges. In contrast, SDAN maintains excellent and stable performance across the entire range of aneurysm diameters, without significant accuracy degradation, fully demonstrating its robust adaptability to the size of IAs and its precise segmentation ability.

## 5.2 Functional analysis of modules

The heatmap is shown in Figure 7. The heatmap results show that when an image is input into ELAM, the output heatmap demonstrates significant attention to the contours of the vascular structure, but the response to IAs is relatively weak. This phenomenon can be attributed to the fact that ELAM constructs local attention through the collaborative mechanism of horizontal and vertical convolutions, making the module highly sensitive to the boundary features within the local window. However, due to the lack of integration of global semantic information, ELAM has difficulty achieving the differential recognition of IAs and vessels. After being processed by GSFB, there is a significant transformation in the attention distribution of the heatmap: the response intensity in the aneurysm area has been greatly enhanced, while the attention to the contours of vascular structure has decreased significantly. This optimization benefits from the fact

that GSFB uses the output features of ELAM as queries and maps them into the global attention mechanism. Under the joint action of spatial and channel dimensions, it can achieve accurate detection of the aneurysm contours and simultaneously suppress interference of vessel characteristics. The relevant evidence will be further demonstrated in the ablation studies.

# 6 Conclusion

In this paper, we introduced a deep learning model named Shape-aware Dual-stream Attention Network (SDAN) for accurate intracranial aneurysm (IA) segmentation from single-frame Digital Subtraction Angiography (DSA). We conducted thorough evaluations using multi-center data. Our experimental results demonstrated that SDAN outperformed all baseline models in all datasets. Crucially, it maintained robust performance, particularly in segmenting small aneurysms. Therefore, this algorithm holds strong potential as an effective auxiliary tool for clinical intracranial aneurysm diagnosis and treatment, thereby enhancing physicians' diagnostic and therapeutic efficiency. Current limitations include slightly reduced performance on external datasets, potentially attributable to variations in image quality across institutions. SDAN is designed based on approaches for small target segmentation (like aneurysm segmentation), and we believe it has the potential to accomplish various small target segmentation tasks. In future work, we will further explore whether this neural network can handle segmentation tasks involving other types or modalities of data.

# Data availability statement

The data analyzed in this study is subject to the following licenses/restrictions: the data cannot be made publicly available upon publication because they are owned by a third party and the terms of use prevent public distribution. The data that support the findings of this study are available upon reasonable request from the authors. Requests to access these datasets should be directed to Ma He, mahe@bmie.neu.edu.cn.

# **Ethics statement**

The studies involving humans were approved by the Ethics Committee of General Hospital of Northern Theater Command. The studies were conducted in accordance with the local legislation and institutional requirements. Written informed consent for participation was not required from the participants or the participants' legal guardians/next of kin in accordance with the national legislation and institutional requirements.

# References

1. Vlak MH, Algra A, Brandenburg R, Rinkel GJ. Prevalence of unruptured intracranial aneurysms, with emphasis on sex, age, comorbidity, country, and time period: a systematic review and meta-analysis. *Lancet Neurol.* (2011) 10:626–36. doi: 10.1016/S1474-4422(11)70109-0

### **Author contributions**

RL: Software, Investigation, Writing – original draft, Conceptualization, Methodology. RZ: Data curation, Investigation, Writing – review & editing, Formal analysis. WQ: Supervision, Writing – review & editing, Resources. GL: Writing – review & editing, Supervision, Formal analysis. GC: Writing – review & editing, Formal analysis, Data curation. HJ: Writing – review & editing, Project administration, Funding acquisition. LC: Writing – review & editing, Visualization, Project administration. JL: Resources, Validation, Writing – review & editing. HM: Supervision, Project administration, Writing – review & editing.

# **Funding**

The author(s) declare that financial support was received for the research and/or publication of this article. This study was supported by both the Science and Technology Planning Project of Liaoning Province, China under Grant 2022JH2/101500037 and 2023JH2/101600017.

### Conflict of interest

The authors declare that the research was conducted in the absence of any commercial or financial relationships that could be construed as a potential conflict of interest.

## Generative AI statement

The author(s) declare that no Gen AI was used in the creation of this manuscript.

Any alternative text (alt text) provided alongside figures in this article has been generated by Frontiers with the support of artificial intelligence and reasonable efforts have been made to ensure accuracy, including review by the authors wherever possible. If you identify any issues, please contact us.

# Publisher's note

All claims expressed in this article are solely those of the authors and do not necessarily represent those of their affiliated organizations, or those of the publisher, the editors and the reviewers. Any product that may be evaluated in this article, or claim that may be made by its manufacturer, is not guaranteed or endorsed by the publisher.

2. de Rooij NK, Linn FH, van der Plas JA, Algra A, Rinkel GJ. Incidence of subarachnoid haemorrhage: a systematic review with emphasis on region, age, gender and time trends. *J Neurol Neurosurg Psychiat.* (2007) 78:1365–72. doi: 10.1136/jnnp.2007.117655

- 3. Etminan N, Rinkel GJ. Unruptured intracranial aneurysms: development, rupture and preventive management. *Nat Rev Neurol.* (2016) 12:699–713. doi: 10.1038/nrneurol.2016.150
- 4. Nieuwkamp DJ, Setz LE, Algra A, Linn FH, de Rooij NK, Rinkel GJ. Changes in case fatality of aneurysmal subarachnoid haemorrhage over time, according to age, sex, and region: a meta-analysis. *Lancet Neurol.* (2009) 8:635–42. doi: 10.1016/S1474-4422(09)70126-7
- 5. Tjoumakaris SI, Hanel R, Mocco J, Ali-Aziz Sultan M, Froehler M, Lieber BB, et al. ARISE I consensus review on the management of intracranial aneurysms. *Stroke*. (2024) 55:1428–37. doi: 10.1161/STROKEAHA.123.046208
- 6. Thilak S, Brown P, Whitehouse T, Gautam N, Lawrence E, Ahmed Z, et al. Diagnosis and management of subarachnoid haemorrhage. *Nat Commun.* (2024) 15:1850. doi: 10.1038/s41467-024-46015-2
- 7. de Barros Pontes FG, da Silva EM, Baptista-Silva JC, Vasconcelos V. Treatments for unruptured intracranial aneurysms. *Cochr Datab System Rev.* (2021) 5:CD013312. doi: 10.1002/14651858.CD013312.pub2
- 8. Wiebers DO. Unruptured intracranial aneurysms: natural history, clinical outcome, and risks of surgical and endovascular treatment. *Lancet.* (2003) 362:103–10. doi: 10.1016/S0140-6736(03)13860-3
- 9. Shi Z, Miao C, Schoepf UJ, Savage RH, Dargis DM, Pan C, et al. A clinically applicable deep-learning model for detecting intracranial aneurysm in computed tomography angiography images. *Nat Commun.* (2020) 11:6090. doi:10.1038/s41467-020-19527-w
- 10. Lubicz B, Levivier M. François O, Thoma P, Sadeghi N, Collignon L, et al. Sixty-four-row multisection CT angiography for detection and evaluation of ruptured intracranial aneurysms: interobserver and intertechnique reproducibility Am J Neuroradiol. (2007) 28:1949–55. doi: 10.3174/ajnr.A0699
- 11. Kancheva AK, Velthuis BK, Ruigrok YM. Imaging markers of intracranial aneurysm development: a systematic review. J Neuroradiol. (2022) 49:219–24. doi: 10.1016/j.neurad.2021.09.001
- 12. Bechan R, Van Rooij S, Sprengers M, Peluso J, Sluzewski M, Majoie C, et al. CT angiography versus 3D rotational angiography in patients with subarachnoid hemorrhage. Neuroradiology. (2015) 57:1239–46. doi: 10.1007/s00234-015-1590-9
- 13. Zeng Y, Liu X, Xiao N, Li Y, Jiang Y, Feng J, et al. Automatic diagnosis based on spatial information fusion feature for intracranial aneurysm. *IEEE Trans Med Imaging*. (2019) 39:1448–58. doi: 10.1109/TMI.2019.2951439
- 14. Pal SC, Toumpanakis D, Wikström J, Ahuja CK, Strand R, Dhara AK. Multi-level residual dual attention network for major cerebral arteries segmentation in MRA toward diagnosis of cerebrovascular disorders. *IEEE Trans NanoBiosci.* (2023) 23:167–75. doi: 10.1109/TNB.2023.3298444
- 15. Pal SC, Toumpanakis D, Wikström J, Ahuja CK, Strand R, Dhara AK. Automated segmentation of post-treatment intracranial aneurysms from MRA images: a u-net based approach. In: 2024 IEEE 21st India Council International Conference (INDICON). IEEE (2024). p. 1–5. doi: 10.1109/INDICON63790.2024.10958485
- 16. Din M, Agarwal S, Grzeda M, Wood DA, Modat M, Booth TC. Detection of cerebral aneurysms using artificial intelligence: a systematic review and meta-analysis. *J Neurointerv Surg.* (2023) 15:262–71. doi: 10.1136/jnis-2022-019456
- 17. Zhou Z, Jin Y, Ye H, Zhang X, Liu J, Zhang W. Classification, detection, and segmentation performance of image-based AI in intracranial aneurysm: a systematic review. *BMC Med Imag.* (2024) 24:164. doi: 10.1186/s12880-024-01347-9
- 18. Jerman T, Pernus F, Likar B, Špiclin Ž. Aneurysm detection in 3D cerebral angiograms based on intra-vascular distance mapping and convolutional neural networks. In: 2017 IEEE 14th International Symposium on Biomedical Imaging (ISBI 2017). IEEE (2017). p. 612–615. doi: 10.1109/ISBI.2017.7950595
- Podgorsak AR, Rava RA, Bhurwani MMS, Chandra AR, Davies JM, Siddiqui AH, et al. Automatic radiomic feature extraction using deep learning for angiographic parametric imaging of intracranial aneurysms. J Neurointerv Surg. (2020) 12:417–21. doi: 10.1136/neurintsurg-2019-015214
- 20. Podgoršak AR, Bhurwani MM, Rava RA, Chandra AR, Ionita CN. Use of a convolutional neural network for aneurysm identification in digital subtraction angiography. In: *Medical Imaging 2019: Computer-Aided Diagnosis*. SPIE (2019). p. 1106–1118. doi: 10.1117/12.2512810
- 21. Duan H, Huang Y, Liu L, Dai H, Chen L, Zhou L. Automatic detection on intracranial aneurysm from digital subtraction angiography with cascade convolutional neural networks. *Biomed Eng Online*. (2019) 18:1–18. doi: 10.1186/s12938-019-0726-2
- 22. Jin H, Geng J, Yin Y, Hu M, Yang G, Xiang S, et al. Fully automated intracranial aneurysm detection and segmentation from digital subtraction angiography series using an end-to-end spatiotemporal deep neural network. *J Neurointerv Surg.* (2020) 12:1023–7. doi: 10.1136/neurintsurg-2020-015824
- 23. Liao J, Liu L, Duan H, Huang Y, Zhou L, Chen L, et al. Using a convolutional neural network and convolutional long short-term memory to automatically detect aneurysms on 2D digital subtraction angiography images: framework development and validation. *JMIR Med Inf.* (2022) 10:e28880. doi: 10.2196/28880

- 24. Bizjak Ž, Špiclin Ž. A systematic review of deep-learning methods for intracranial aneurysm detection in CT angiography. *Biomedicines*. (2023) 11:2921. doi: 10.3390/biomedicines11112921
- 25. Hsu WC, Meuschke M, Frangi AF, Preim B, Lawonn K. A survey of intracranial aneurysm detection and segmentation. *Med Image Anal.* (2025) 101:103493. doi: 10.1016/j.media.2025.103493
- 26. Zhang M, Zhang C, Wu X, Cao X, Young GS, Chen H, et al. A neural network approach to segment brain blood vessels in digital subtraction angiography. *Comput Methods Programs Biomed.* (2020) 185:105159. doi: 10.1016/j.cmpb.2019.105159
- 27. Qu J, Niu H, Li Y, Chen T, Peng F, Xia J, et al. A deep learning framework for intracranial aneurysms automatic segmentation and detection on magnetic resonance T1 images. *Eur Radiol.* (2024) 34:2838–48. doi: 10.1007/s00330-023-10295-x
- 28. Zhang J, Zhao Y, Liu X, Jiang J, Li Y. FSTIF-UNet: a deep learning-based method towards automatic segmentation of intracranial aneurysms in un-reconstructed 3D-RA. *IEEE J Biomed Health Inf.* (2023) 27:4028–39. doi: 10.1109/JBHI.2023.3278472
- 29. Liu X, Feng J, Wu Z, Neo Z, Zhu C, Zhang P, et al. Deep neural network-based detection and segmentation of intracranial aneurysms on 3D rotational DSA. *Interv Neuroradiol.* (2021) 27:648–57. doi: 10.1177/15910199211000956
- 30. Park A, Chute C, Rajpurkar P, Lou J, Ball RL, Shpanskaya K, et al. Deep learning-assisted diagnosis of cerebral aneurysms using the HeadXNet model. *JAMA Netw Open.* (2019) 2:e195600–e195600. doi: 10.1001/jamanetworkopen.2019.5600
- 31. Shao D, Lu X, Liu X. 3D intracranial aneurysm classification and segmentation via unsupervised Dual-branch learning. *IEEE J Biomed Health Inform.* (2022) 27:1770–9. doi: 10.1109/JBHI.2022.3180326
- 32. Yuan W, Peng Y, Guo Y, Ren Y, Xue Q. DCAU-Net: dense convolutional attention U-Net for segmentation of intracranial aneurysm images. *Visual Comput Ind Biomed Art.* (2022) 5:9. doi: 10.1186/s42492-022-00105-4
- 33. Zhu W, Li W, Tian Z, Zhang Y, Wang K, Zhang Y, et al. Stability assessment of intracranial aneurysms using machine learning based on clinical and morphological features. *Transl Stroke Res.* (2020) 11:1287–95. doi: 10.1007/s12975-020-00811-2
- 34. Backes D, Rinkel GJ, Greving JP, Velthuis BK, Murayama Y, Takao H, et al. ELAPSS score for prediction of risk of growth of unruptured intracranial aneurysms. *Neurology*. (2017) 88:1600–6. doi: 10.1212/WNL.000000000003865
- 35. Pal SC, Toumpanakis D, Wikström J, Ahuja CK, Strand R, Dhara AK. Context-aware preprocessing method for reduction of volume of interest towards quantification of pre and post-treatment intracranial aneurysms in MRA. In: International Conference on Pattern Recognition. Springer (2024). p. 233–242. doi: 10.1007/978-3-031-88220-3\_17
- 36. Abdullah I, Javed A, Malik KM, Malik G. DeepInfusion: a dynamic infusion based-neuro-symbolic AI model for segmentation of intracranial aneurysms. *Neurocomputing*. (2023) 551:126510. doi: 10.1016/j.neucom.2023.126510
- 37. Mo Y, Chen Y, Hu Y, Xu J, Wang H, Dai L, et al. Focusing intracranial aneurysm lesion segmentation by graph Mask2Former with local refinement in DSA images. In: 2023 IEEE International Conference on Bioinformatics and Biomedicine (BIBM). IEEE (2023). p. 899–903. doi: 10.1109/BIBM58861.2023.10385276
- 38. Mu N, Lyu Z, Rezaeitaleshmahalleh M, Tang J, Jiang J. An attention residual u-net with differential preprocessing and geometric postprocessing: learning how to segment vasculature including intracranial aneurysms. *Med Image Anal.* (2023) 84:102697. doi: 10.1016/j.media.2022.102697
- 39. Tang H, Chen Y, Wang T, Zhou Y, Zhao L, Gao Q, et al. HTC-Net: A hybrid CNN-transformer framework for medical image segmentation. *Biomed Signal Process Control.* (2024) 88:105605. doi: 10.1016/j.bspc.2023.105605
- 40. Wang W, Xie E, Li X, Fan DP, Song K, Liang D, et al. Pvt v2: improved baselines with pyramid vision transformer. *Comput Visual Media*. (2022) 8:415–24. doi: 10.1007/s41095-022-0274-8
- 41. Liu Y, Shao Z, Hoffmann N. Global attention mechanism: retain information to enhance channel-spatial interactions. *arXiv preprint arXiv:211205561*. (2021).
- 42. Abbasi M, Saeedi P. Enhancing multivariate time series classifiers through self-attention and relative positioning infusion. *IEEE Access.* (2024) 12:67273–67290. doi: 10.1109/ACCESS.2024.3397783
- Ming Z, Berrio JS, Shan M, Worrall S. Inversematrixvt3d: an efficient projection matrix-based approach for 3D occupancy prediction. In: 2024 IEEE/RSJ International Conference on Intelligent Robots and Systems (IROS). IEEE (2024). p. 9565–9572. doi: 10.1109/IROS58592.2024.10802434
- 44. Loshchilov I, Hutter F. Decoupled weight decay regularization. arXiv preprint arXiv:171105101. (2017).
- 45. Ronneberger O, Fischer P, Brox T. U-net: convolutional networks for biomedical image segmentation. In: Medical image computing and computer-assisted intervention-MICCAI 2015: 18th international conference, Munich, Germany, October 5-9, 2015, proceedings, part III 18. Springer (2015). p. 234–241. doi: 10.1007/978-3-319-24574-4\_28
- 46. Peng Y, Sonka M, Chen DZ. U-net v2: rethinking the skip connections of u-net for medical image segmentation. *arXiv preprint arXiv:231117791*. (2023).

- 47. Oktay O, Schlemper J, Folgoc LL, Lee M, Heinrich M, Misawa K, et al. Attention u-net: learning where to look for the pancreas. *arXiv preprint arXiv:180403999*. (2018).
- 48. Isensee F, Jaeger PF, Kohl SA, Petersen J, Maier-Hein KH. nnU-Net: a self-configuring method for deep learning-based biomedical image segmentation. *Nat Methods*. (2021) 18:203–11. doi: 10.1038/s41592-020-01 008-z
- 49. Badrinarayanan V, Kendall A, Cipolla R. Segnet: a deep convolutional encoder-decoder architecture for image segmentation. *IEEE Trans Pattern Anal Mach Intell.* (2017) 39:2481–95. doi: 10.1109/TPAMI.2016.2644615
- 50. Hatamizadeh A, Tang Y, Nath V, Yang D, Myronenko A, Landman B, et al. UNETR: transformers for 3D medical image segmentation. In: *Proceedings of the IEEE/CVF Winter Conference on Applications of Computer Vision* (2022). p. 574–584. doi: 10.1109/WACV51458.2022.00181
- 51. Cao H, Wang Y, Chen J, Jiang D, Zhang X, Tian Q, et al. Swin-unet: Unetlike pure transformer for medical image segmentation. In:  $European\ Conference$

- on Computer Vision. Springer (2022). p. 205–218. doi: 10.1007/978-3-031-250 66-8\_9
- 52. Hatamizadeh A, Nath V, Tang Y, Yang D, Roth HR, Xu D. Swin UNETR: Swin transformers for semantic segmentation of brain tumors in MRI images. In: *International MICCAI Brainlesion Workshop*. Springer (2021). p. 272–284. doi: 10.1007/978-3-031-08999-2\_22
- 53. Ruan J, Li J, Xiang S. Vm-unet: vision mamba uNet for medical image segmentation. arXiv preprint arXiv:240202491. (2024). doi: 10.1145/3767748
- 54. Zhang M, Yu Y, Jin S, Gu L, Ling T, Tao X. VM-UNET-V2: rethinking vision mamba UNet for medical image segmentation. In: *International Symposium on Bioinformatics Research and Applications*. Springer (2024). p. 335–346. doi: 10.1007/978-981-97-5128-0\_27
- 55. Hu J, Shen L, Sun G. Squeeze-and-excitation networks. In: *Proceedings of the IEEE Conference on Computer Vision and Pattern Recognition* (2018). p. 7132–7141. doi: 10.1109/CVPR.2018.00745